

- completeness = 98.7% (91.6 from 2.11 to 2.05 Å),  $R_{\text{merge}} = \sum_i \sum_j |I_{hkl} - \langle I_{hkl} \rangle| / \sum_i \sum_j I_{hkl} = 5.5\%$ , where  $h$  are unique reflections indices and  $i$  indicate symmetry equivalent indices. Refinement calculations:  $R_{\text{factor}} = (\sum |F_o - F_c|) / \sum F_o = 18.8\%$ , where  $F_o$  and  $F_c$  are the observed and calculated structure factors, respectively;  $R_{\text{free}} = 26.4\%$  (same calculation as for  $R_{\text{factor}}$ , but with 5% of the data); average atomic  $B$  values for protein: 31.4 Å<sup>2</sup>, inhibitor = 32.2 Å<sup>2</sup>, waters = 37.7 Å<sup>2</sup>. Observed deviations: root means square (rms) bond lengths = 0.008 Å; rms bond angles = 1.31°. The final model includes 279 residues of CDK2 (residues 36 to 43 and 153 to 163 are not included because of weak or missing electron density), purvalanol B, 91 water molecules, and one molecule of ethyleneglycol. Efforts to crystallize the CDK2-purvalanol A complex resulted crystals of poor quality.
13. M. C. Wahl and M. Sundaralingam, *Trends Biochem. Sci.* **22**, 97 (1997).
  14. E. E. Brooks et al., *J. Biol. Chem.* **272**, 29207 (1997).
  15. Because of weak inhibition of yeast growth by flavopiridol we used a strain with three drug-sensitizing deletions ( $\Delta\text{erg6}$ ,  $\Delta\text{pdr5}$ ,  $\Delta\text{snq2}$ ). This strain showed  $\text{GI}_{50}$  for **52** and flavopiridol at concentrations of 30 and 7 μM, respectively. Three cultures [110 ml, in yeast extract, peptone, and dextrose (YPD)] were inoculated with single colonies of YRP1 (*MATα*,  $\Delta\text{erg6}::\text{LEU2}$ ,  $\Delta\text{pdr5}::\text{TRP1}$ ,  $\Delta\text{snq2}::\text{HIS6}$ ) and grown at 30°C with constant agitation in a water bath incubator. When the cell density reached an optical density (OD) of 0.9 (at a wavelength of 600 nm), 27.5 μl of a 100 mM dimethyl sulfoxide (DMSO) stock solution of **52** or flavopiridol or DMSO alone was added. After 2 hours the cells were harvested by centrifugation and flash frozen with liquid nitrogen. For the temperature-sensitive *cdc28* mutants, three cultures (75 ml, YPD) of AFS199 (*cdc28-13*), AA104 (*cdc28-4*), and their isogenic background strain AFS34 (*MATα*, *ade2-1*, *his3-11*, *leu2-3*, *trp1-1*, *ura3*) were grown from single colonies to an OD of 0.9 (600 nm) and harvested as described. Frozen cells were stored at -80°C.
  16. The diminished growth inhibitory activity of compound **52Me** is unlikely to result from poorer bio-availability because a similar N6 methylation is observed to increase the in vivo potency of a related series of purine-based inhibitors. The residual growth inhibitory activity of **52Me** likely reflects activity against other cellular targets. Compounds **52**, **52Me**, and flavopiridol failed to cause a uniform arrest morphology in yeast. FACS analysis also did not reveal synchronization of yeast cells after treatment with **52** or **52Me**, which may be due to inhibition of a variety of CDKs responsible for different cell cycle transitions (as is observed in FACS experiments on mammalian cells) or activity against other targets not specifically examined in vitro.
  17. D. J. Lockhart et al., *Nature Biotechnol.* **14**, 1675 (1996).
  18. L. Wodicka, H. Dong, M. Mittmann, M.-H. Ho, D. J. Lockhart, *ibid.* **15**, 1359 (1997).
  19. J. L. DeRisi, V. R. Iyer, P. O. Brown, *Science* **278**, 680 (1997).
  20. S. P. A. Fodor et al., *ibid.* **251**, 767 (1991).
  21. Transcripts that showed a significant and reproducible change in concentration (greater than twofold) in cells treated with the compounds between triplicate hybridizations for each of at least two independent experiments were examined further.
  22. F. R. Cross, *Curr. Opin. Cell Biol.* **7**, 790 (1995).
  23. A. J. Van Wijnen et al., *Proc. Natl. Acad. Sci. U.S.A.* **91**, 12882 (1994).
  24. E. M. Lenburg and E. K. O'Shea, *Trends Biol. Sci.* **V21** 383 (1996).
  25. L. W. Bergman and B. K. Timblin, *Mol. Microbiol.* **26**, 981 (1997).
  26. L. W. Bergman, K. Tatchell, B. K. Timblin, *Genetics* **143**, 57 (1996).
  27. Because the *PHO85* gene is nonessential it should be possible to determine if these inductions are a direct consequence of Pho85p kinase inhibition by determining if the same inductions are seen after treating with inhibitor in a strain lacking the kinase.
  28. B. Andrews et al., *Mol. Cell Biol.* **17**, 1212 (1997).
  29. P. Mazur et al., *ibid.* **15**, 5671 (1995).
  30. Transcript profiles were also measured for the *cdc28* temperature-sensitive allele *cdc28-13*. The *cdc28-13* strain contains an arginine to asparagine mutation at residue 283 near the COOH-terminus, which does not significantly affect kinase activity at the permissive temperature but does cause cell cycle arrest when switched to the nonpermissive temperature (32). The *cdc28-13* strain showed very few changes in mRNA transcripts when compared with wild type at the permissive temperature. The levels of only 11 mRNAs changed by more than twofold, consistent with the observation that this mutant has essentially wild-type kinase activity at 25°C. In addition, the nearly identical gene expression patterns obtained for the *cdc28-13* and isogenic wild-type *CDK28* strain demonstrate the reproducibility of these experiments.
  31. The *cdc28-4* allele that exhibits a START ( $G_1$ -S) defect or an allele such as *cdc28-1N*, which has a  $G_2$ -M defect could also serve as a mimic of CDK inhibition by **52** or flavopiridol.
  32. S. I. Reed, J. A. Hadwiger, A. T. Lorincz, *Proc. Natl. Acad. Sci. U.S.A.* **82**, 4055 (1985).
  33. C. Koch and K. Nasmyth, *Curr. Opin. Cell Biol.* **6**, 451 (1994).
  34. M. Russell, J. Bradshaw-Rouse, D. Markwardt, W. Heidemman, *Mol. Biol. Cell* **4**, 757 (1993).
  35. H. Ruis and C. Schuller, *BioEssays* **17**, 959 (1995).
  36. J. R. Woodgett et al., *Trends Biochem. Sci.* **16**, 177 (1991).
  37. U.S. Patent Application 1368.002
  38. For example, using a screen of our purine libraries, to be described elsewhere, we have identified a compound that causes extensive depolymerization of microtubules and condensation of DNA.
  39. J. Rine, W. Hansen, E. Hardeman, R. W. Davis, *Proc. Natl. Acad. Sci. U.S.A.* **80**, 6750 (1983); M. Schena, D. Shalon, R.W. Davis, P. O. Brown, *Science* **270**, 467 (1995).
  40. We thank A. Murray for providing the CDC28 temperature-sensitive strains and for helpful discussions, C. Mimotopes for providing derivatized pins, D. Drubin and members of his lab, the National Cancer Institute for performing cellular screens, and M.-H. Ho for help with expression data analysis. Supported by the Director, Office of Health Effects Research of the U.S. Department of Energy (to S.-H. K. and P.C.S.), the Association pour la Recherche sur le Cancer (ARC9157 to L.M.), the Conseil Regional de Bretagne (to L.M.), and the CaP Cure Foundation. N.S.G. is supported by a NSF predoctoral fellowship and A.-M.T. by a long-term fellowship from the Human Frontier Science Program. The coordinates have been deposited with Protein Data Bank with ID code 1CKP.

22 April 1998; accepted 4 June 1998

## Synthesis of Macroporous Minerals with Highly Ordered Three-Dimensional Arrays of Spheroidal Voids

Brian T. Holland, Christopher F. Blanford, Andreas Stein\*

Titania, zirconia, and alumina samples with periodic three-dimensional arrays of macropores were synthesized from the corresponding metal alkoxides, using latex spheres as templates. In a fast, single-step reaction, the monomeric alkoxide precursors permeate the array of bulk polystyrene spheres and condense in air at room temperature. Close packed, open-pore structures with 320- to 360-nanometer voids are obtained after calcination of the organic component at 575°C. The examples presented demonstrate the compositional diversity possible with this technique. The resulting highly structured ceramics could have applications in areas ranging from quantum electronics to photocatalysis to battery materials.

The use of organic templates to control the structure of inorganic solids has proven very successful for designing porous materials with pore sizes ranging from angstroms to micrometers. In the case of microporous silicates and aluminosilicates, the organic additives are molecular and lead to zeolitic structures. Larger mesopores are obtained by using surfactant arrays or emulsion droplets as templates (1-4). Recent reports illustrate that techniques using latex spheres or block-copolymers can be used to create silica structures with pore sizes ranging from 5 nm to 1 μm (5-8). Porous solids have made a great

impact in applications including catalysis, sorption, and separations (9). Advanced optoelectronics applications that would benefit from a facile method of producing large quantities of porous materials in various compositions with high degrees of three-dimensional (3D) order have been proposed (10). For example, quantum electronics and optical communications require single-mode microcavities constructed from dielectric materials with adjustable composition and multidimensional periodicity (11). So far, the fabrication of such structures with periodicity in three dimensions and feature sizes below 1 μm has remained an experimental challenge (12). Catalysis and large-molecule separation processes would also benefit from more uniform porous supports that provide optimal flow and improved efficiencies (13, 14).

Department of Chemistry, University of Minnesota, Minneapolis, MN 55455, USA.

\*To whom correspondence should be addressed. E-mail: stein@chem.umn.edu

## REPORTS

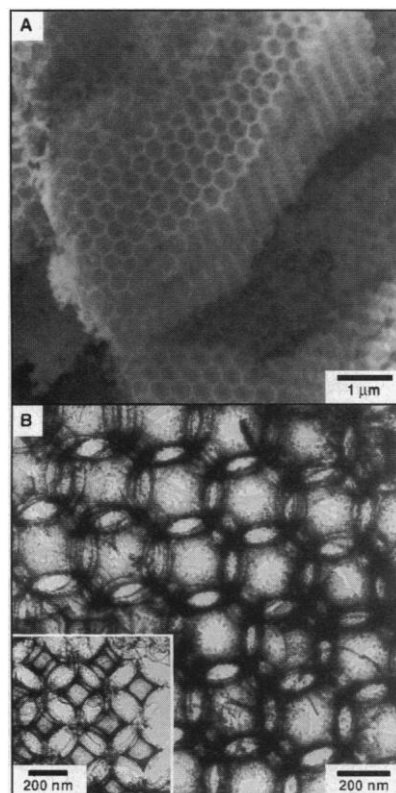


**Fig. 1.** (A) SEM image showing the inorganic skeleton of a typical macroporous zirconium oxide particle after calcination. Multiple hexagonal void planes are interconnected to form a pseudocrystalline lattice. (B) TEM image of the same sample, showing the inorganic replica (dark regions) of several layers of close packed spheres. The baddeleyite microcrystallites composing the framework can be seen on the edges of the dark regions. Selected-area electron diffraction (SAED) patterns of the microcrystallites matched the bulk PXRD patterns. Inset: Projection of a different particle displaying 4mm symmetry.

We discovered that latex particle templating can be used to create macroporous networks of numerous oxide compositions in a simple, rapid, surfactant-free process. The materials generated from this process exhibit remarkable 3D ordering of the pores. The metal oxides are synthesized from readily available metal alkoxide precursors that are typically used in sol-gel chemistry (15). The technique requires no pretreatment or special handling of many metal alkoxides, even for a reactive metal alkoxide like titanium ethoxide. The versatility of the process is exemplified by the synthesis of porous titania (a photoreactive, large-bandgap semiconductor in bulk form), alumina (a catalyst or chromatographic support), and zirconia (a highly corrosion-resistant ceramic). A tremendous impact can be expected in applications that rely on porosity, low density, and 3D order in ceramic structures.

Nearly monodisperse latex spheres with

**Table 1.** Physical properties of the macroporous solids. BET surface areas were determined from nitrogen adsorption measurements carried out on an RXM-100 sorption system (Advanced Scientific Designs, Grosse Pointe Park, MI). Average microcrystalline particle sizes were estimated from the BET surface areas, assuming spherical particles and from the peak broadening in PXRD patterns, using the Scherrer equation. Mercury porosimetry measurements, carried out on a Micromeritics Poresizer 9320, indicated a total intrusion volume of 0.66 ml/g and a median pore diameter of 269 nm for the macroporous ZrO<sub>2</sub> sample.

Sample (phase)	BET surface area (m <sup>2</sup> /g)	Wall thickness (nm) TEM	Microcrystalline particle size (nm)		
			TEM	BET	PXRD
ZrO <sub>2</sub> (baddeleyite)	38	8–13	9–13	13	26–30
TiO <sub>2</sub> (anatase)	22	24–36	20–35	35	34
Al <sub>2</sub> O <sub>3</sub> · xH <sub>2</sub> O* (amorphous)	317	4–6	No microcrystals		

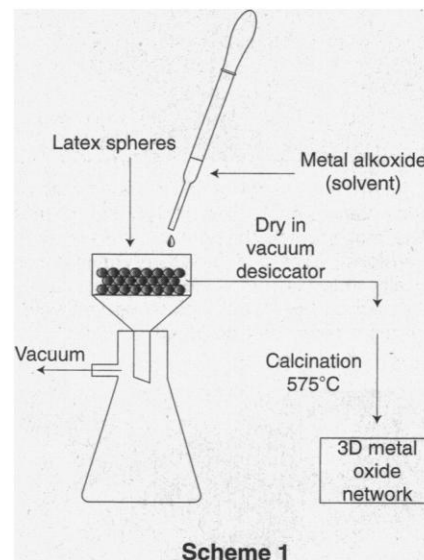
\* x ≈ 0.9 from H-analysis (Atlantic Microlab, Norcross, GA).

an average diameter of 470 nm were synthesized by emulsifier-free emulsion polymerization (16). Styrene (inhibitor removed) was polymerized in degassed water at 70°C, using potassium persulfate as an initiator. No surfactant was used as a stabilizer. Monodispersity was achieved by maintaining a constant temperature and stir rate (245 rpm) throughout the 28-hour reaction. The latex spheres were centrifuged, air dried, and used directly in the subsequent templating reactions.

Scheme 1 illustrates the simple synthesis of the macroporous metal oxide networks. Millimeter-thick layers of latex spheres were deposited on filter paper in a Buchner funnel under vacuum and soaked with ethanol (or 2-butanol for the aluminum alkoxide). Titanium ethoxide, zirconium *n*-propoxide, or aluminum tri-*sec*-butoxide was added dropwise to cover the latex spheres completely while suction was applied. Typical mass ratios of alkoxide to latex were between 1.4 and 3. After drying the composite in a vacuum desiccator for 3 to 24 hours, the latex spheres were removed by calcination in flowing air at 575°C for 7 to 12 hours, leaving hard and brittle powder particles with 320- to 360-nm voids. The carbon content of the calcined samples varied from 0.4 to 1.0 wt %, indicating that most of the latex templates had been removed from the 3D host. All samples underwent shrinkage during calcination. The center-to-center separations between cavities were 26 to 32% smaller than the diameters of the original latex spheres.

Scanning electron micrographs (Figs. 1A and 2) show that the close packing order of the latex spheres was imprinted into the ceramic matrix (17). Large fractions of the calcined sample were highly ordered in three dimensions over a range of hundreds of micrometers, resembling cubic close packing of cages. The remaining portions exhibited similar uniform porosity with hexagonal close packing or less regular packing of voids. The void spaces were interconnected

in three dimensions through windows whose diameters typically exceeded 100 nm. Ordering of the pores increased with increasing flow rate of metal alkoxide and decreasing humidity. For more viscous reagents (aluminum tri-*sec*-butoxide) the alkoxide was diluted in the corresponding alcohol (2-butanol, 50/50 wt/wt). In contrast to the procedures described previously (5, 6), surfactant stabilizers were not necessary to create close packing of the hybrid latex-inorganic composite. In fact, addition of surfactant appeared to reduce the average structural order of the products.



The inorganic oxide phases were identified by powder x-ray diffraction (PXRD) of the bulk sample and by electron diffraction (ED) in the TEM on several ordered areas (Table 1). The bulk macroporous zirconia and titania samples were crystalline, with networks composed of fused microcrystallites (Fig. 1B). The measured Brunauer-Emmett-Teller (BET) surface areas of these materials were mostly due to the small particle size of the crystallites, in agreement with size estimates from TEM images and from PXRD peak broadening.

## REPORTS

The calcined macroporous alumina was amorphous, exhibiting a considerably higher surface area than the zirconia or titania samples. The walls of this sample appeared to be amorphous films by ED and TEM (Fig. 3), yet the 3D packing of the macropores in this sample was similar to that for zirconia and titania. The wall thicknesses, estimated from TEM, varied significantly among the three samples. It is likely that wall thicknesses depend on the individual crystallization kinetics, as well as on any interactions between the latex templates and the inorganic components.

Preliminary experiments have shown that this technique of creating 3D ordered macroporous structures can easily be adapted to oxides of other metals (such as iron and tungsten), phosphates (such as aluminophosphate), and possibly chalcogenides (18). It is

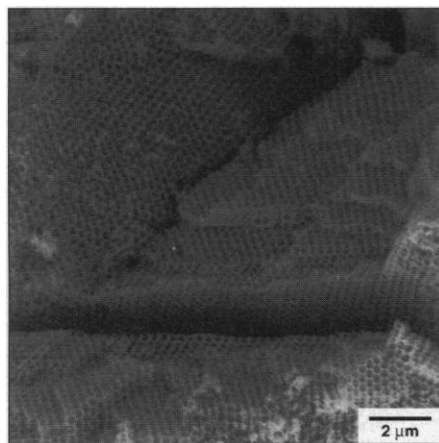


**Fig. 2.** An SEM image of the calcined macroporous titania sample. The crevice in the center of the image reveals the pore structure in three dimensions. Steps and facets resemble those typically found in crystalline structures. Facets composed of hexagonally close packed voids were most commonly observed.

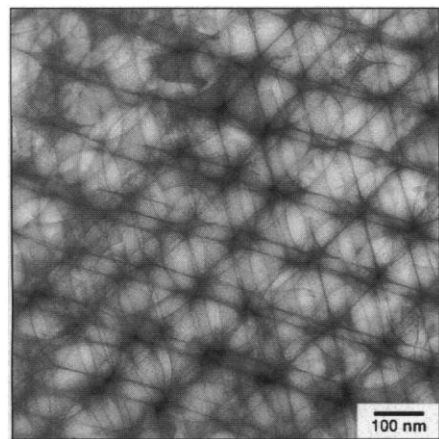


**Fig. 3.** TEM image of the calcined macroporous alumina sample. No crystalline particles are observed either from bulk PXRD patterns or from SAED patterns.

also possible to create hybrid organic-inorganic wall compositions by using organoalkoxysilanes as precursors, similar to the direct synthesis of mesoporous sieves (19). The ease, reproducibility, and versatility of this synthetic approach will facilitate development of new materials and the examination of their structure-property relations. We anticipate that the technique can be modified to include different template sizes. The simplicity of the method suggests that it is amenable to commercial scale-up. Foreseeable technological applications of these materials include quantum optics or optical communications, chromatography, large-molecule catalysis, host-guest systems, thermal or electrical insulators, composites, and porous electrodes or electrolytes.

### References and Notes

1. C. T. Kresge, M. E. Leonowicz, W. J. Roth, J. C. Vartuli, J. S. Beck, *Nature* **359**, 710 (1992).
2. A. Monnier *et al.*, *Science* **261**, 1299 (1993).
3. Q. Huo *et al.*, *Nature* **368**, 317 (1994).
4. A. Imhof and D. J. Pine, *ibid.* **389**, 948 (1997).
5. O. D. Velev, T. A. Jede, R. F. Lobo, A. M. Lenhoff, *ibid.* **389**, 447 (1997).
6. M. Antonietti, B. Berton, C. Göltner, H. P. Hentze, *Adv. Mater.* **10**, 154 (1998).
7. M. Templin *et al.*, *Science* **278**, 1795 (1997).
8. D. Zhao *et al.*, *ibid.* **279**, 548 (1998).
9. J. C. Jansen, M. Stöcker, H. G. Karge, J. Weitkamp, Eds.,

*Advanced Zeolite Science and Applications* (Elsevier, Amsterdam, 1994).

10. C. A. Ozin, *Adv. Mater.* **4**, 612 (1992).
11. E. Yablonovitch, *J. Opt. Soc. Am. B* **10**, 283 (1993).
12. J. D. Joannopoulos, P. R. Villeneuve, S. Fan, *Nature* **386**, 143 (1997).
13. R. H. Perry and D. Green, Eds., *Perry's Chemical Engineers' Handbook* (McGraw-Hill, New York, 1984).
14. M. T. W. Hearn, Ed., *HPLC of Proteins, Peptides and Polynucleotides* (VCH, New York, 1991).
15. C. J. Brinker and G. W. Scherer, *Sol-Gel Science: The Physics and Chemistry of Sol-Gel Processing* (Academic Press, San Diego, CA, 1990).
16. R. L. Fedie, thesis, University of Minnesota, Minneapolis (1996).
17. Scanning electron microscope (SEM) images were recorded digitally on a JEOL 840 SEM operating at 7 kV. Samples were coated with 50 Å of Pt or Pd/Au. Transmission electron microscope (TEM) images were recorded on film on a Philips CM30 TEM operating at 300 kV. Samples were sonicated for 30 min in ethanol and deposited on a holey carbon grid.
18. C. F. Blanford, B. T. Holland, A. Stein, unpublished results.
19. M. H. Lim, C. F. Blanford, A. Stein, *J. Am. Chem. Soc.* **119**, 4090 (1997); *Chem. Mater.* **10**, 467 (1998).
20. Acknowledgment is made to 3M, Dupont, the David and Lucille Packard Foundation, the McKnight Foundation, and NSF (DMR-9701507) for support of this research. We thank W. G. Miller and D. G. Gold for assistance with the latex sphere preparation, and W. L. Gladfelter and M. D. Ward for helpful discussions. B.T.H. and C.F.B. thank the Center for Interfacial Engineering (CIE) at the University of Minnesota for a CIE-NSF graduate fellowship.

7 April 1998; accepted 5 June 1998

## A Tunable Kondo Effect in Quantum Dots

Sara M. Cronenwett, Tjerk H. Oosterkamp, Leo P. Kouwenhoven

A tunable Kondo effect has been realized in small quantum dots. A dot can be switched from a Kondo system to a non-Kondo system as the number of electrons on the dot is changed from odd to even. The Kondo temperature can be tuned by means of a gate voltage as a single-particle energy state nears the Fermi energy. Measurements of the temperature and magnetic field dependence of a Coulomb-blockaded dot show good agreement with predictions of both equilibrium and nonequilibrium Kondo effects.

Quantum dots are small solid-state devices in which the number of electrons can be made a well-defined integer  $N$ . The electronic states in dots can be probed by transport when a small tunnel coupling is allowed between the dot and nearby source and drain leads. This coupling is usually made as weak as possible to prevent strong fluctuations in the number of confined electrons. A well-defined number of electrons also implies a definite confined charge, that is,  $N$  times the elementary charge

$e$ . The quantization of charge permits the use of a simple model in which all of the electron-electron interactions are captured in the single-electron charging energy  $e^2/C$ , where  $C$  is the capacitance of the dot. This simple model has been successful in describing the transport phenomena generally known as single-electron transport and Coulomb blockade effects (1).

If the tunnel coupling to the leads is increased, the number of electrons on the dot becomes less well defined. When the fluctuations in  $N$  become much greater than unity, the quantization of charge is completely lost. In this open regime, theories of noninteracting electrons usually give a proper description of transport. The theory is more complicated in the intermediate regime where the tunnel coupling is relatively strong but the

S. M. Cronenwett, Department of Applied Physics and DIMES, Delft University of Technology, Post Office Box 5046, 2600 GA Delft, Netherlands, and Department of Physics, Stanford University, Stanford, CA, 94305-4060, USA. T. H. Oosterkamp and L. P. Kouwenhoven, Department of Applied Physics and DIMES, Delft University of Technology, Post Office Box 5046, 2600 GA Delft, Netherlands.